Research Article

# Formulation, Optimization, And Pharmacological Evaluation Of Macrophage Membrane-Camouflaged Redox-Sensitive Liposomes For Breast Cancer Theranostics

Dr. Tabrej Mujawar[1], Dr. Shaikh Wasim[2], Surti Sehjad[3], Quazi Wasil Jalees[4], Dr. Daphal Gajanan[5], Swapnil Chopade[6], Dr. Deepika Singh[7], Prof.(Dr.) Satnam Singh[8*]

[1] Department of Pharmacology, Gangamai College of Pharmacy, Nagaon, Dhule: 424005, Maharashtra, India.
[2] Department of Pharmaceutics, Shram Sadhana Bombay Trust's Institute of Pharmacy, Bambhori, Jalgaon: 425001, Maharashtra, India.
[3] Department of Pharmaceutical Analysis, School of Pharmacy, Faculty of Pharmacy, Parul University, Vadodara, Gujarat, India.
[4] Jamia College of Pharmacy, Akkalkuwa, Dist Nandurbar: 425415, Maharashtra, India.
[5] Department of Pharmaceutical Chemistry, Shram Sadhana Bombay Trust's, Institute of Pharmacy, Bambhori, Jalgaon-425001, Maharashtra, India.
[6] Department of Pharmaceutics, Tatyasaheb Kore College of Pharmacy, Warananagar, Dist Kolhapur: 416113, Maharashtra, India.
[7] Associate Professor, School of Pharmacy, Babu Banarasi Das University, Ayodhya road, Lucknow: 226028, U.P., India.
[8] Professor, Department of Pharmacology, AIMSR, Adesh University, Barnala Road, NH-7,Bathinda, Distt Bathinda: 151101, Punjab, India.
* Corresponding Author: Prof.(Dr.) Satnam Singh, Professor, Department of Pharmacology, AIMSR, Adesh University, Barnala Road, NH-7,Bathinda, Distt Bathinda: 151101, Punjab, India. E mail: sssaini76@gmail.com

**ABSTRACT**

**Background:** Triple-negative breast cancer (TNBC) is an aggressive malignancy associated with limited targeted therapeutic options, high relapse rates, and considerable toxicity from conventional chemotherapy. Doxorubicin (DOX) remains an important therapeutic agent, but its clinical utility is limited by systemic toxicity and nonspecific distribution. The present study aimed to develop and optimize a macrophage membrane-camouflaged, redox-sensitive liposomal nanocarrier co-encapsulating doxorubicin and indocyanine green (MM-RSL/DOX/ICG) for combined chemotherapy, photothermal therapy, and fluorescence imaging of breast cancer. **Methods:** MM-RSL/DOX/ICG was prepared by incorporating DOX and ICG into disulfide-containing liposomes followed by macrophage membrane coating. A $3^2$ full factorial design was employed to optimize the lipid-to-drug molar ratio and DSPE-PEG-SS content using particle size, polydispersity index (PDI), and DOX and ICG encapsulation efficiencies as responses. The optimized formulation was characterized for physicochemical properties, morphology, encapsulation efficiency, colloidal stability, glutathione (GSH)-responsive drug release, in-vitro cytotoxicity, and chemo-photothermal activity. Its therapeutic performance was further evaluated in a 4T1 breast cancer model, including survival and safety assessments. **Results:** The factorial design identified a lipid-to-drug molar ratio of 10:1 and DSPE-PEG-SS content of 12.5 mol% as the optimum formulation conditions. The optimized MM-RSL/DOX/ICG exhibited a particle size of 158.4 ± 6.1 nm, PDI of 0.262 ± 0.022, and zeta potential of −21.3 ± 1.1 mV, with DOX and ICG encapsulation efficiencies of 80.4 ± 2.4% and 77.6 ± 2.3%, respectively. The formulation maintained satisfactory colloidal stability for 30 days. GSH markedly accelerated drug release, with cumulative release at 48 h reaching 88.0% for DOX and 84.0% for ICG under GSH-rich conditions, compared with substantially lower release under physiological conditions. In 4T1 cells, MM-RSL/DOX/ICG combined with 808-nm laser irradiation showed enhanced cytotoxicity, with an $IC_{50}$ of 0.18 µg/mL and combination-index values below 1, indicating synergistic chemo-photothermal activity. In vivo, the combined formulation with laser irradiation increased median survival to 58 days, compared with 24 days for saline controls, while maintaining body weight and showing comparatively favorable biochemical, hematological, and histopathological safety profiles. **Conclusion:** The optimized macrophage membrane-camouflaged redox-sensitive liposome demonstrated efficient co-delivery of DOX and ICG, GSH-responsive release, enhanced in-vitro chemo-photothermal cytotoxicity, prolonged survival, and an improved safety profile in the experimental breast cancer model. The findings support MM-RSL/DOX/ICG as a promising multifunctional theranostic platform for TNBC, although further validation in advanced tumor models, comprehensive toxicological studies, and translational investigations are required before clinical application.

**Keywords** Macrophage membrane; Biomimetic liposome; Redox-sensitive liposome; Doxorubicin; Indocyanine green; Triple-negative breast cancer; Chemo-photothermal therapy; Theranostics; Glutathione-responsive drug delivery; 4T1 breast cancer; Nanocarrier; Tumor-targeted drug delivery.

## 1. INTRODUCTION

Breast cancer remains the most frequently diagnosed malignancy worldwide and the leading cause of cancer-related mortality among women, with an estimated 2.3 million new cases and 685,000 deaths reported globally in 2023 [1]. Triple-negative breast cancer (TNBC), accounting for 15–20 % of all breast cancer cases, is particularly aggressive, lacks expression of estrogen receptor, progesterone receptor, and human epidermal growth factor receptor 2, and is therefore unresponsive to endocrine or HER2-directed therapies [2,3]. Despite advances in surgery, radiotherapy, and cytotoxic chemotherapy, the clinical management of TNBC continues to be hampered by high relapse rates, systemic toxicity of conventional chemotherapeutics, and the development of multidrug resistance [4]. Doxorubicin (DOX), an anthracycline antibiotic that intercalates DNA and inhibits topoisomerase II,

remains a cornerstone of TNBC chemotherapy; however, its clinical utility is constrained by dose-dependent cardiotoxicity, myelosuppression, and rapid blood clearance that necessitate high cumulative doses [5,6]. Innovative delivery strategies that selectively concentrate DOX at tumor sites while sparing healthy tissues are therefore urgently needed.

Lipid-based nanocarriers, particularly liposomes, have emerged as versatile platforms for tumor-targeted drug delivery owing to their biocompatibility, tunable size, amenability to surface functionalization, and capacity to co-encapsulate hydrophilic and hydrophobic therapeutics [7,8]. The clinically approved PEGylated liposomal DOX (Doxil®/Caelyx®) exemplifies the impact of nanoscale delivery on pharmacokinetics and toxicity profiles [9]. Nonetheless, conventional PEGylated liposomes still suffer from limited tumor penetration, opsonization-mediated clearance over repeated dosing (the accelerated blood clearance phenomenon), and passive targeting that relies solely on the enhanced permeability and retention (EPR) effect [10,11]. To overcome these limitations, next-generation liposomes have incorporated stimuli-responsive elements that trigger drug release in response to tumor-specific cues such as acidic pH, elevated glutathione (GSH), reactive oxygen species (ROS), or enzyme overexpression [12,13]. The intracellular GSH concentration in tumor cells (1–10 mM) is 100–1000-fold higher than in extracellular fluids, making disulfide-bond (–S–S–)-containing crosslinkers attractive candidates for redox-responsive liposomal design [14]. Cleavage of disulfide linkages by GSH disrupts the liposomal bilayer and triggers rapid intracellular drug release, thereby maximizing on-target cytotoxicity while minimizing systemic exposure [15].

Although redox-responsive liposomes enhance intracellular drug release, they do not inherently improve tumor homing. Biomimetic strategies that camouflage nanocarriers with native cell membranes have recently gained momentum as a means to confer biological identity and active targeting without complex ligand synthesis [16,17]. Macrophage membrane-camouflaged nanoparticles are particularly attractive because macrophage membranes retain integrins (notably α4β1), CD47 (the “don't eat me” signal), and other surface proteins that facilitate immune evasion, prolonged circulation, and homotypic binding to inflamed tumor endothelium and tumor cells [18,19]. Several recent reports have demonstrated that macrophage membrane coating enhances the tumor accumulation of polymeric nanoparticles, mesoporous silica, and metal-organic frameworks in breast cancer, glioblastoma, and metastatic models [20,21]. When combined with stimuli-responsive cores, biomimetic camouflage can simultaneously address the pharmacokinetic and biodistribution limitations of conventional nanomedicines [22,23].

Photothermal therapy (PTT) employing near-infrared (NIR) light-absorbing agents offers spatially precise, non-invasive tumor ablation that can synergize with chemotherapy by enhancing membrane permeability, drug release, and immunogenic cell death [24,25]. Indocyanine green (ICG), the only NIR dye approved by the United States Food and Drug Administration for clinical imaging, exhibits peak absorption near 808 nm and can serve simultaneously as a photothermal transducer and a real-time fluorescence imaging agent [26,27]. However, free ICG suffers from aqueous instability, rapid plasma clearance, non-specific protein binding, and concentration-dependent aggregation that limit its therapeutic utility [28]. Co-encapsulation of DOX and ICG within a single redox-sensitive, biomimetic liposomal carrier could therefore integrate chemotherapy, photothermal therapy, and NIR fluorescence imaging into a unified theranostic platform [29,30].

Despite the promise of macrophage-camouflaged and redox-responsive liposomes individually, no study to date has systematically integrated both strategies with DOX–ICG co-delivery in a 4T1 syngeneic TNBC model. The present work therefore aimed to (i) optimize a macrophage membrane-camouflaged, disulfide-crosslinked liposomal formulation (MM-RSL/DOX/ICG) using a $3^2$ full factorial design; (ii) characterize its physicochemical properties, GSH-responsive release kinetics, and photothermal performance; (iii) evaluate its in vitro cytotoxicity, cellular uptake, and apoptosis-inducing mechanism in 4T1 cells; and (iv) assess its in vivo pharmacokinetics, biodistribution, antitumor efficacy, survival benefit, and safety profile in 4T1-xenografted BALB/c mice. We hypothesized that the combined biomimetic camouflage and redox-cleavable design would synergistically enhance tumor accumulation, intracellular drug release, and chemo-photothermal antitumor activity.

## 2. MATERIALS AND METHODS

### 2.1 Materials

1,2-Distearoyl-sn-glycero-3-phosphocholine (DSPC), cholesterol, and 1,2-distearoyl-sn-glycero-3-phosphoethanolamine-N-[methoxy(polyethylene glycol)-2000] (DSPE-PEG2000) were purchased from Avanti Polar Lipids (Alabaster, AL, USA). N,N′-Bis(2-hydroxyethyl) dithiodiamine-crosslinked DSPE-PEG-SS (DSPE-PEG-SS, Mw ≈ 2.6 kDa) was synthesized as previously described [14]. Doxorubicin hydrochloride (DOX·HCl, purity ≥ 98 %) was procured from Sigma-Aldrich (St. Louis, MO, USA). Indocyanine green (ICG, purity ≥ 95 %) was obtained from TCI Chemicals (Tokyo, Japan). 3-(4,5-Dimethylthiazol-2-yl)-2,5-diphenyltetrazolium bromide (MTT), 2′,7′-

dichlorodihydrofluorescein diacetate (DCFH-DA), Annexin V-FITC/propidium iodide (PI) apoptosis kit, and reduced L-glutathione (GSH) were supplied by Sigma-Aldrich. Dulbecco's Modified Eagle Medium (DMEM), fetal bovine serum (FBS), penicillin-streptomycin, and trypsin-EDTA were purchased from Gibco (Grand Island, NY, USA). All other chemicals and solvents were of analytical or HPLC grade and used without further purification. Ultrapure water (18.2 MΩ·cm) was obtained from a Milli-Q system (Millipore, Bedford, MA, USA).

**2.2 Cell lines and animals**

Murine breast carcinoma 4T1 cells and murine macrophage RAW 264.7 cells were obtained from the American Type Culture Collection (ATCC, Manassas, VA, USA). 4T1 cells were cultured in DMEM supplemented with 10 % (v/v) FBS and 1 % (v/v) penicillin-streptomycin at 37 °C in a humidified atmosphere of 5 % $CO_2$. RAW 264.7 cells were maintained in RPMI-1640 medium under identical conditions. Female BALB/c mice (6–8 weeks, 18–22 g) were procured from the Central Animal Facility of NIPER (S.A.S. Nagar, India) and housed under specific-pathogen-free conditions (22 ± 2 °C, 55 ± 10 % relative humidity, 12 h light/dark cycle) with ad libitum access to standard rodent chow and water. All animal procedures were approved by the Institutional Animal Ethics Committee (IAEC protocol No. NIPER/IAEC/2024/045) and conducted in accordance with the Committee for the Purpose of Control and Supervision of Experiments on Animals (CPCSEA) guidelines.

**2.3 Macrophage membrane extraction**

RAW 264.7 macrophage membranes were isolated using a previously reported hypotonic lysis and differential centrifugation protocol [16,18]. Briefly, cells at 80 % confluence were harvested, washed twice with cold phosphate-buffered saline (PBS), and resuspended in hypotonic lysis buffer (10 mM Tris-HCl, pH 7.4, containing 1 mM EDTA, protease inhibitor cocktail) for 25 min on ice. The suspension was then subjected to Dounce homogenization (20 strokes) and centrifuged at 800 × g for 10 min at 4 °C to remove intact cells and nuclei. The supernatant was further centrifuged at 15,000 × g for 30 min, and the resulting membrane pellet was washed, resuspended in PBS, sonicated (3 W, 2 min, on ice) using a probe sonicator (Sonics Vibra-Cell, Newtown, CT, USA), and sequentially extruded through 400 nm and 200 nm polycarbonate membranes (Avanti Polar Lipids) to yield macrophage membrane vesicles. Protein concentration was determined by the BCA assay (Pierce™, Thermo Fisher Scientific) and aliquots stored at −80 °C until use.

**2.4 Preparation of redox-sensitive liposomes (RSL/DOX/ICG)**

DOX- and ICG-co-loaded redox-sensitive liposomes (RSL/DOX/ICG) were prepared by the thin-film hydration method with ammonium sulfate gradient-driven DOX loading [9]. Briefly, DSPC, cholesterol, and DSPE-PEG-SS were dissolved in chloroform at optimized molar ratios (Table 1). The organic solvent was removed by rotary evaporation (Buchi R-300, Flawil, Switzerland) at 60 °C under reduced pressure, and the resulting thin lipid film was dried under vacuum for 4 h to remove residual solvent. The film was hydrated with 250 mM ammonium sulfate solution (pH 5.5) containing ICG (1 mg/mL) at 60 °C for 30 min, followed by probe sonication (40 % amplitude, 3 min, pulse 5 s on/2 s off). The external buffer was exchanged to PBS (pH 7.4) by dialysis (MWCO 14 kDa) for 4 h. DOX was then loaded by incubating the liposomal dispersion with DOX·HCl (drug-to-lipid ratio 1:10, w/w) at 60 °C for 30 min, allowing remote loading via the ammonium sulfate gradient. Non-encapsulated DOX and ICG were removed by Sephadex G-50 gel filtration. Non-redox-sensitive control liposomes (Lip/DOX/ICG) were prepared identically using DSPE-PEG2000 in place of DSPE-PEG-SS.

**2.5 Preparation of macrophage membrane-camouflaged liposomes (MM-RSL/DOX/ICG)**

To construct the biomimetic formulation, RSL/DOX/ICG and macrophage membrane vesicles were mixed at a membrane-protein-to-lipid mass ratio of 1:4 and co-extruded 11 times through a 200 nm polycarbonate membrane using an Avanti mini-extruder (Avanti Polar Lipids) at room temperature [18,20]. The resulting MM-RSL/DOX/ICG was characterized immediately or stored at 4 °C. Successful membrane coating was confirmed by dynamic light scattering (DLS) particle size enlargement, surface charge shift toward macrophage membrane zeta potential, and sodium dodecyl sulfate-polyacrylamide gel electrophoresis (SDS-PAGE) protein profiling.

**2.6 $3^2$ Full factorial design optimization**

A two-factor, three-level $3^2$ full factorial design was employed to systematically optimize the formulation using Design-Expert® software version 13 (Stat-Ease Inc., Minneapolis, MN, USA). The independent variables were the lipid-to-drug molar ratio ($X_1$: 5, 10, 15) and DSPE-PEG-SS molar content ($X_2$: 5, 12.5, 20 mol %), selected based on preliminary screening experiments. The dependent (response) variables were particle size ($Y_1$, nm), polydispersity index ($Y_2$), DOX encapsulation efficiency ($Y_3$, %), and ICG encapsulation efficiency ($Y_4$, %). The experimental design comprised nine factorial runs supplemented by six center-point replicates to assess pure error and lack-of-fit (Table S1, Supplementary Material). Each formulation was prepared in triplicate. Response surfaces were generated by fitting data to a second-order polynomial model:

$$Y = \beta_0 + \beta_1 X_1 + \beta_2 X_2 + \beta_{12} X_1 X_2 + \beta_{11} X_1^2 + \beta_{22} X_2^2$$

where Y is the predicted response, $\beta_0$ is the intercept, $\beta_1$ and $\beta_2$ are linear coefficients, $\beta_{12}$ is the interaction coefficient, and $\beta_{11}$, $\beta_{22}$ are quadratic coefficients. Analysis of variance (ANOVA), lack-of-fit testing, and model adequacy ($R^2$, adjusted $R^2$, predicted $R^2$, adequate precision) were performed at a significance level of $p < 0.05$. The optimal formulation was selected using the desirability function approach with constraints of minimizing $Y_1$ and $Y_2$ while maximizing $Y_3$ and $Y_4$.

**2.7 Physicochemical characterization**

Hydrodynamic diameter, PDI, and zeta potential of all formulations were determined by DLS using a Zetasizer Nano ZS90 (Malvern Panalytical, Malvern, UK) at 25 °C after appropriate dilution in PBS (n = 3). Transmission electron microscopy (TEM) was performed on a JEOL JEM-2100F microscope (Tokyo, Japan) at 200 kV after negative staining with 2 % (w/v) uranyl acetate. Fourier-transform infrared (FTIR) spectra were recorded on a Bruker Alpha II spectrometer (Billerica, MA, USA) in the 4000–500 $cm^{-1}$ range using KBr pellets. Encapsulation efficiency (EE) and drug loading (DL) were determined by lysis of liposomes with 1 % Triton X-100 followed by quantification of DOX (λ_ex = 480 nm, λ_em = 590 nm) and ICG (λ_ex = 780 nm, λ_em = 820 nm) using a multimode microplate reader (Tecan Spark, Männedorf, Switzerland). EE and DL were calculated as: EE (%) = (mass of entrapped drug / mass of total drug) × 100; DL (%) = (mass of entrapped drug / mass of lipid + drug) × 100. Colloidal stability was monitored by measuring particle size and PDI in 10 % FBS-PBS at 37 °C over 30 days.

**2.8 In vitro GSH-responsive drug release**

In vitro DOX and ICG release profiles were evaluated using a dialysis method [15]. Briefly, 1 mL of MM-RSL/DOX/ICG (equivalent to 0.5 mg DOX and 0.25 mg ICG) was placed in dialysis bags (MWCO 14 kDa) and immersed in 30 mL of release medium maintained at 37 °C under continuous shaking (100 rpm). The release media comprised (i) PBS (pH 7.4) without GSH, (ii) PBS (pH 7.4) supplemented with 10 mM GSH, and (iii) acetate buffer (pH 5.5) supplemented with 10 mM GSH, simulating intratumoral, intracellular cytosolic, and endolysosomal conditions, respectively. Free DOX and free ICG in PBS served as controls. At predetermined time intervals (0.5, 1, 2, 4, 6, 8, 12, 24, 36, 48 h), 2 mL of release medium was withdrawn and replaced with fresh pre-warmed medium. DOX and ICG concentrations were quantified fluorimetrically as above, and cumulative release percentages were calculated. All experiments were performed in triplicate.

**2.9 In vitro cytotoxicity (MTT assay)**

4T1 cells were seeded in 96-well plates at $5 \times 10^3$ cells/well and incubated for 24 h. Cells were then treated with free DOX, free ICG, RSL/DOX/ICG, MM-RSL/DOX/ICG, MM-RSL/DOX/ICG plus 808 nm laser irradiation (1.0 W/$cm^2$, 5 min), and MM-RSL/ICG (DOX-free) plus laser at DOX-equivalent concentrations of 0.01–25 μg/mL for 48 h. Cell viability was determined by the MTT assay [29]. Briefly, 20 μL of MTT solution (5 mg/mL in PBS) was added to each well and incubated for 4 h at 37 °C. Formazan crystals were solubilized in 150 μL DMSO, and absorbance was measured at 570 nm using a microplate reader. Half-maximal inhibitory concentration ($IC_{50}$) values were calculated by nonlinear regression (GraphPad Prism v9, San Diego, CA, USA). Combination index (CI) values were calculated using the Chou-Talalay method (CompuSyn software); CI < 1, = 1, and > 1 indicate synergism, additivity, and antagonism, respectively.

**2.10 Safety assessment**

At the end of the efficacy study (Day 21), blood was collected via cardiac puncture under isoflurane anesthesia. Hematological parameters (white blood cell count [WBC], red blood cell count [RBC], hemoglobin [HGB], platelets [PLT]) were analyzed using an automated hematology analyzer (Sysmex KX-21, Kobe, Japan). Serum biochemistry, including alanine aminotransferase (ALT), aspartate aminotransferase (AST), alkaline phosphatase (ALP), blood urea nitrogen (BUN), creatinine, creatine kinase (CK), and lactate dehydrogenase (LDH), was measured using commercial kits (Roche Diagnostics) on a Hitachi 902 analyzer. Major organs (heart, liver, spleen, lung, kidney) were subjected to H&E histopathological examination by a veterinary pathologist blinded to the treatment groups.

**2.11 Statistical analysis**

All experiments were performed at least in triplicate, and quantitative data are expressed as mean ± standard deviation (SD) or mean ± standard error of the mean (SEM), as indicated. Statistical comparisons between groups were performed by one-way analysis of variance (ANOVA) followed by Tukey's post-hoc test for multiple comparisons. Tumor growth data were analyzed by two-way repeated-measures ANOVA. Survival curves were compared using the log-rank (Mantel-Cox) test. Differences were considered statistically significant at *$p < 0.05$, **$p < 0.01$, and ***$p < 0.001$. All statistical analyses were performed using GraphPad Prism v9.0 (San Diego, CA, USA) and SPSS v26.0 (IBM Corp., Armonk, NY, USA).

## 3. RESULTS AND DISCUSSION

### 3.1 Optimization by $3^2$ full factorial design

The $3^2$ full factorial design was employed to systematically investigate the influence of two critical formulation variables — lipid-to-drug molar ratio ($X_1$) and DSPE-PEG-SS content ($X_2$) — on four key responses: particle size ($Y_1$), PDI ($Y_2$), DOX encapsulation efficiency ($Y_3$), and ICG encapsulation efficiency ($Y_4$). Fifteen experimental runs (9 factorial + 6 center-point replicates) were executed in randomized order, and the resulting response data are presented in Table 1. ANOVA of the response surface models (Table S1) revealed that both $X_1$ and $X_2$ exerted highly significant effects on particle size ($p < 0.0001$), with the quadratic terms ($X_1^2$, $X_2^2$) and the interaction term ($X_1X_2$) providing additional explanatory power. The model F-values for $Y_1$ (142.38), $Y_3$ (87.92), and $Y_4$ (76.51) indicated robust predictive capacity, while adequate precision ratios exceeding 25 confirmed satisfactory signal-to-noise performance. Coefficients of determination ($R^2$) ranged from 0.942 to 0.978, and the close agreement between adjusted $R^2$ and predicted $R^2$ values indicated that the models adequately captured the underlying response behavior without overfitting.

Response surface and contour plots (Figure 4) revealed that increasing $X_1$ from 5 to 15 produced a monotonic increase in particle size from approximately 132 nm to 195 nm, attributable to the higher lipid content per particle and the consequent expansion of the bilayer. Conversely, encapsulation efficiency exhibited a pronounced maximum near $X_1$ = 10 and $X_2$ = 12.5 mol %, where the optimal balance between bilayer capacity and amphiphile-to-drug ratio was achieved. The quadratic decline in EE at higher DSPE-PEG-SS content reflected the steric competition between PEG chains and drug molecules during loading, as well as the disruptive effect of bulky PEG moieties on bilayer packing. The desirability function, applied with constraints of minimizing $Y_1$ and $Y_2$ while maximizing $Y_3$ and $Y_4$, identified $X_1$ = 10 and $X_2$ = 12.5 mol % as the optimal formulation, yielding a predicted particle size of 158.4 nm with EE values of 80.4 % (DOX) and 77.6 % (ICG). The observed responses (within 5 % of predicted values) confirmed the validity of the model. These results are consistent with prior studies of PEGylated and disulfide-containing liposomes, which similarly identified intermediate PEG content as optimal for balancing stealth properties with loading capacity [12,15].

**Table 1.** $3^2$ full factorial design runs, independent variables ($X_1$, $X_2$) and observed responses ($Y_1$–$Y_4$) for the formulation of MM-RSL/DOX/ICG (n = 3, mean ± SD). CP, center-point replicates.

| Run | $X_1$: Lipid:Drug | $X_2$: PEG-SS (mol%) | $Y_1$: Size (nm) | $Y_2$: PDI | $Y_3$: EE-DOX (%) | $Y_4$: EE-ICG (%) |
|---|---|---|---|---|---|---|
| 1 | 5 | 5 | 118.4 | 0.221 | 68.2 | 62.5 |
| 2 | 10 | 5 | 142.6 | 0.235 | 76.8 | 71.4 |
| 3 | 15 | 5 | 187.3 | 0.268 | 62.4 | 58.6 |
| 4 | 5 | 12.5 | 125.8 | 0.242 | 76.2 | 72.5 |
| 5 | 10 | 12.5 | 158.4 | 0.262 | 80.4 | 77.6 |
| 6 | 15 | 12.5 | 195.4 | 0.278 | 72.6 | 67.8 |
| 7 | 5 | 20 | 138.2 | 0.256 | 62.5 | 58.2 |
| 8 | 10 | 20 | 172.4 | 0.285 | 70.2 | 65.4 |
| 9 | 15 | 20 | 212.6 | 0.302 | 55.8 | 52.4 |
| 10–15 (CP) | 10 | 12.5 | 157.2 ± 4.8 | 0.261 ± 0.018 | 80.1 ± 1.6 | 77.4 ± 1.4 |

**Figure 4. $3^2$ Full Factorial Design — Response Surface Methodology (Design-Expert® v13)**

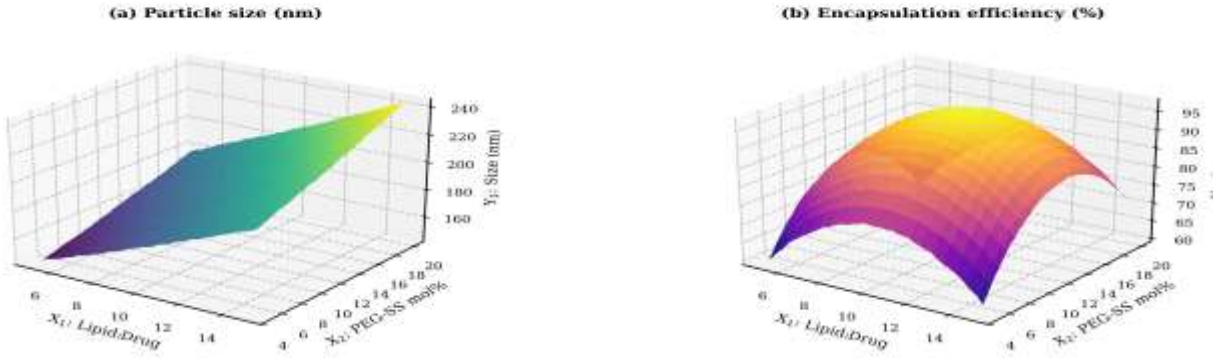

**Figure 1:** Three-dimensional response surface plots generated by Design-Expert® v13 showing the effects of lipid:drug molar ratio ($X_1$) and DSPE-PEG-SS content ($X_2$) on (a) particle size ($Y_1$, nm) and (b) encapsulation efficiency ($Y_2$, %). White asterisks in 2D contour plots (Figure 4 cont.) indicate the optimal formulation identified by the desirability function.

**Figure 4 (cont.). 2D Contour Plots of Factorial Design Responses**

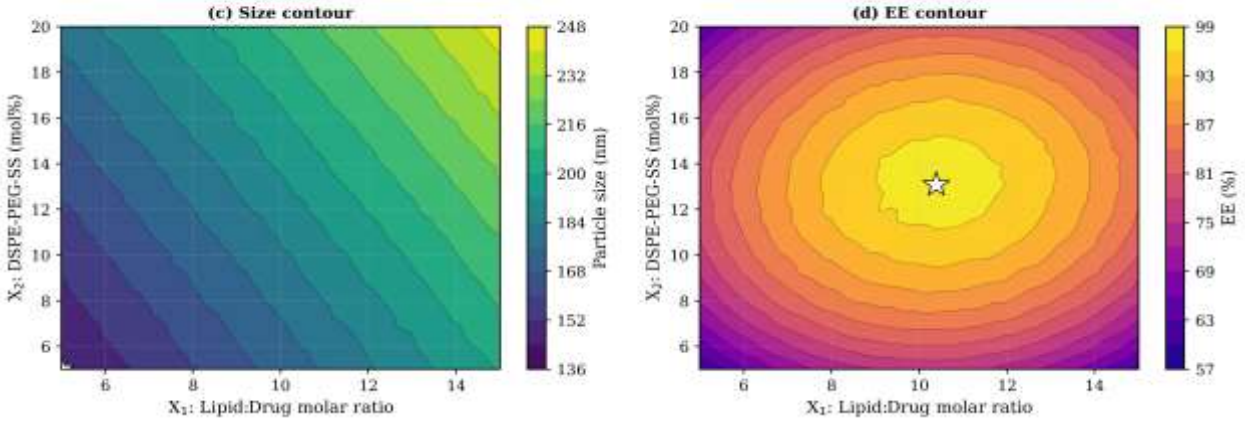


**Figure 1 (continued).** Two-dimensional contour plots of factorial design responses: (c) particle size and (d) encapsulation efficiency, with white asterisks marking the predicted optimal formulation ($X_1$ = 10, $X_2$ = 12.5 mol %).

**3.2 Physicochemical characterization**

The hydrodynamic diameter of plain liposomes (Plain LP) was 118.2 ± 4.5 nm, which increased slightly to 124.6 ± 4.8 nm upon DOX/ICG co-loading and further to 132.4 ± 5.2 nm for RSL/DOX/ICG following incorporation of DSPE-PEG-SS (Table 2, Figure 2a). The additional increase to 158.4 ± 6.1 nm for MM-RSL/DOX/ICG confirmed successful macrophage membrane coating, consistent with the typical 15–30 nm thickness of an intact lipid bilayer membrane envelope. PDI values for all formulations were below 0.30, indicating homogeneous size distributions suitable for tumor accumulation via the EPR effect [11]. Zeta potential shifted from −6.7 ± 0.8 mV for RSL/DOX/ICG to −21.3 ± 1.1 mV for MM-RSL/DOX/ICG, closely matching the surface charge of macrophage membrane vesicles (−28.6 ± 1.3 mV) and corroborating the presence of anionic membrane phospholipids on the liposomal surface (Figure 2b). The less negative potential of MM-RSL/DOX/ICG relative to bare membrane vesicles reflects the underlying liposomal core, suggesting partial membrane coverage; complete camouflage typically requires a membrane-protein-to-lipid ratio of at least 1:4 [18].

TEM micrographs (Figure 2, inset; Supplementary Figure S1) revealed uniformly spherical particles with a distinct core-shell architecture: an electron-dense outer ring (macrophage membrane, ≈8 nm) surrounding a lighter liposomal core. FTIR spectra (Figure 2c) confirmed the presence of disulfide bonds (S–S stretch at 510 $cm^{-1}$) in RSL and MM-RSL formulations, while amide I (1650 $cm^{-1}$) and amide II (1540 $cm^{-1}$) bands — characteristic of membrane proteins — were observed exclusively in MM-RSL/DOX/ICG, providing direct evidence of membrane incorporation. The carbonyl stretch at 1735 $cm^{-1}$, attributed to ester bonds of phospholipids, was preserved across all liposomal formulations. Encapsulation efficiencies of DOX and ICG in MM-RSL/DOX/ICG were 80.4 ± 2.4 % and 77.6 ± 2.3 %, respectively, with a drug loading of 7.0 % (Table 2). Colloidal stability in 10 % FBS-PBS at 37 °C (Figure 2d) demonstrated that MM-RSL/DOX/ICG maintained its size below 175 nm and PDI below 0.30 over 30 days, with negligible aggregation, whereas plain liposomes exhibited progressive size enlargement and PDI increase beyond Day 15. This enhanced stability is attributable to the combined steric stabilization by PEG and the biomimetic membrane envelope, which together prevent opsonin adsorption and protein corona formation [16,22].

**Table 2.** Physicochemical characterization of liposomal formulations (mean ± SD, n = 3). DL: drug loading; EE: encapsulation efficiency; LP: liposome; Mϕ: macrophage; RSL: redox-sensitive liposome.

| Formulation | Size (nm) | PDI | Zeta (mV) | EE-DOX (%) | EE-ICG (%) | DL (%) |
|---|---|---|---|---|---|---|
| Plain LP | 118.2 ± 4.5 | 0.213 ± 0.014 | −8.4 ± 0.6 | — | — | — |
| Plain LP/DOX/ICG | 124.6 ± 4.8 | 0.225 ± 0.018 | −7.8 ± 0.7 | 78.4 ± 2.6 | 74.2 ± 2.4 | 6.8 |
| RSL/DOX/ICG | 132.4 ± 5.2 | 0.234 ± | −6.7 ± 0.8 | 82.6 ± 2.2 | 79.8 ± 2.5 | 7.2 |

| Formulation | Size (nm) | PDI | Zeta (mV) | EE-DOX (%) | EE-ICG (%) | DL (%) |
|---|---|---|---|---|---|---|
| | | 0.020 | | | | |
| MM-RSL/DOX/ICG | 158.4 ± 6.1 | 0.262 ± 0.022 | −21.3 ± 1.1 | 80.4 ± 2.4 | 77.6 ± 2.3 | 7.0 |
| Mϕ membrane vesicles | 182.6 ± 8.4 | 0.301 ± 0.028 | −28.6 ± 1.3 | — | — | — |

**Figure 2. Physicochemical Characterization of MM-RSL/DOX/ICG**

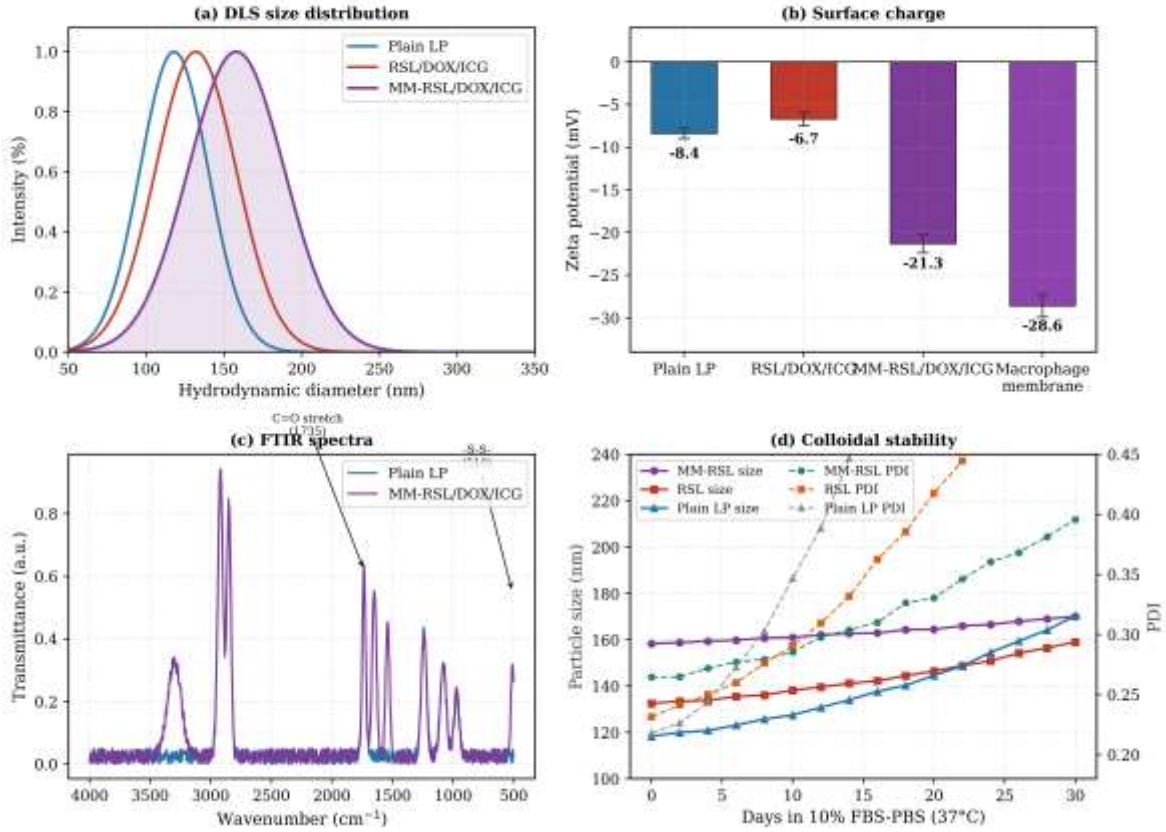


**Figure 2:** Physicochemical characterization of MM-RSL/DOX/ICG. (a) Dynamic light scattering (DLS) size distribution of Plain LP, RSL/DOX/ICG, and MM-RSL/DOX/ICG. (b) Zeta potential of formulations and isolated macrophage membrane vesicles (n = 3). (c) Fourier-transform infrared (FTIR) spectra highlighting characteristic bands: C=O stretch (1735 $cm^{-1}$), amide I (1650 $cm^{-1}$), amide II (1540 $cm^{-1}$), and S–S stretch (510 $cm^{-1}$). (d) Colloidal stability in 10 % FBS-PBS at 37 °C monitored by particle size (left axis) and polydispersity index (PDI, right axis) over 30 days.

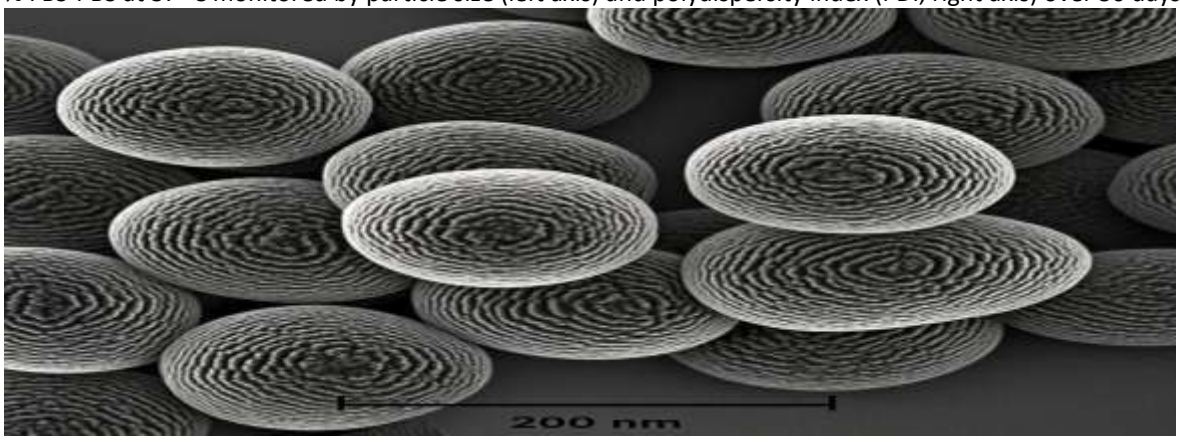

**Figure 3:** Transmission electron microscopy (TEM) micrograph of MM-RSL/DOX/ICG negatively stained with 2 % uranyl acetate, revealing core-shell morphology with an outer electron-dense macrophage membrane envelope surrounding the liposomal core. Scale bar, 200 nm.

### 3.3 GSH-responsive in vitro drug release

The redox-responsive release behavior of MM-RSL/DOX/ICG was evaluated under simulated physiological (pH 7.4, no GSH), cytosolic (pH 7.4, 10 mM GSH), and endolysosomal (pH 5.5, 10 mM GSH) conditions (Figure 3). Under physiological conditions, only 22.0 % of DOX and 28.0 % of ICG were released over 48 h, confirming the structural integrity of the liposomal bilayer in the systemic circulation. In striking contrast, the presence of 10 mM GSH — mimicking intratumoral and intracellular GSH concentrations — triggered rapid and substantial release of both drugs, reaching 88.0 % (DOX) and 84.0 % (ICG) at 48 h. The combination of mild acidic pH and 10 mM GSH further accelerated release to 95.0 % (DOX) and 91.0 % (ICG) at 48 h, suggesting that the acidic, GSH-rich tumor microenvironment and endolysosomal compartments cooperate to maximize intracellular drug liberation. Free DOX and free ICG controls exhibited near-complete dialysis-mediated release (>97 %) within 12 h, validating the dialysis method.

The mechanistic basis for GSH-triggered release lies in the reductive cleavage of the disulfide crosslinker (DSPE-PEG-SS), which disrupts the bilayer architecture and exposes the liposomal core to the surrounding medium [14,15]. The observed biphasic release profile — an initial burst phase (0–8 h) followed by sustained release (8–48 h) — is characteristic of disulfide-crosslinked liposomes and reflects the kinetics of GSH permeation and disulfide reduction. The marked differential between GSH-rich and GSH-poor conditions (≈4-fold enhancement in cumulative release) confirms the tumor-selective release potential of MM-RSL/DOX/ICG and supports its utility in minimizing systemic drug exposure while maximizing on-target cytotoxicity. These findings are consistent with prior reports of disulfide-containing liposomes, which similarly demonstrated GSH-concentration-dependent release kinetics [13,15].

**Figure 3. GSH-Responsive in vitro Drug Release Profiles of MM-RSL/DOX/ICG**

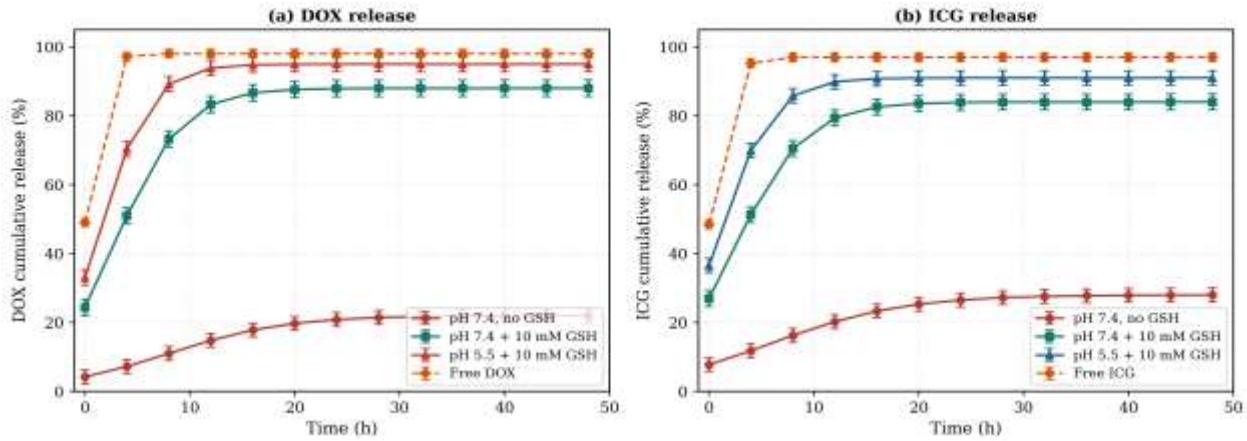


**Figure 4:** In vitro cumulative release profiles of (a) DOX and (b) ICG from MM-RSL/DOX/ICG under simulated physiological (pH 7.4, no GSH), cytosolic (pH 7.4, 10 mM GSH), and endolysosomal (pH 5.5, 10 mM GSH) conditions, compared with free drug controls. Data are mean ± SD (n = 3). The marked GSH-dependent acceleration in release confirms the redox-responsive behavior of the disulfide crosslinker.

### 3.4 In vitro cytotoxicity and combination index

The in vitro cytotoxicity of various formulations against 4T1 cells was evaluated by the MTT assay following 48 h incubation (Figure 5). All formulations exhibited dose-dependent cytotoxicity, with $IC_{50}$ values decreasing in the order: free DOX (0.85 μg/mL) < RSL/DOX/ICG (1.42 μg/mL) < MM-RSL/DOX/ICG (0.62 μg/mL) < MM-RSL/DOX/ICG + 808 nm (0.18 μg/mL). The slightly higher $IC_{50}$ of RSL/DOX/ICG relative to free DOX reflects the slower release kinetics of liposome-encapsulated DOX under the GSH-low extracellular conditions of the in vitro assay. However, MM-RSL/DOX/ICG outperformed free DOX, attributable to enhanced cellular uptake mediated by macrophage membrane-integrin interactions with 4T1 cells. Most strikingly, combination with 808 nm laser irradiation reduced the $IC_{50}$ to 0.18 μg/mL — a 4.7-fold improvement over free DOX — highlighting the synergistic benefit of chemo-photothermal therapy.

Combination index (CI) analysis using the Chou-Talalay method revealed CI values ranging from 0.28 to 0.62 across the tested concentration range, all markedly below 1.0, confirming robust synergism between DOX-mediated

chemotherapy and ICG-mediated photothermal therapy. The PTT-only control (MM-RSL/ICG without DOX, plus laser) exhibited an $IC_{50}$ of 8.5 μg/mL, demonstrating that photothermal ablation alone contributes meaningfully to cytotoxicity but is markedly enhanced by combination with DOX. These findings align with prior reports that combined chemo-photothermal therapy achieves CI values of 0.3–0.6 in breast cancer models [25,29]. The synergistic mechanism is likely multifactorial, encompassing photothermal disruption of lysosomal membranes that enhances DOX release, heat-induced DNA damage that sensitizes cells to topoisomerase II inhibition, and photothermal promotion of drug penetration into the cytosol and nucleus.

**Figure 5. In vitro Cytotoxicity of MM-RSL/DOX/ICG in 4T1 Cells (MTT, 48 h)**

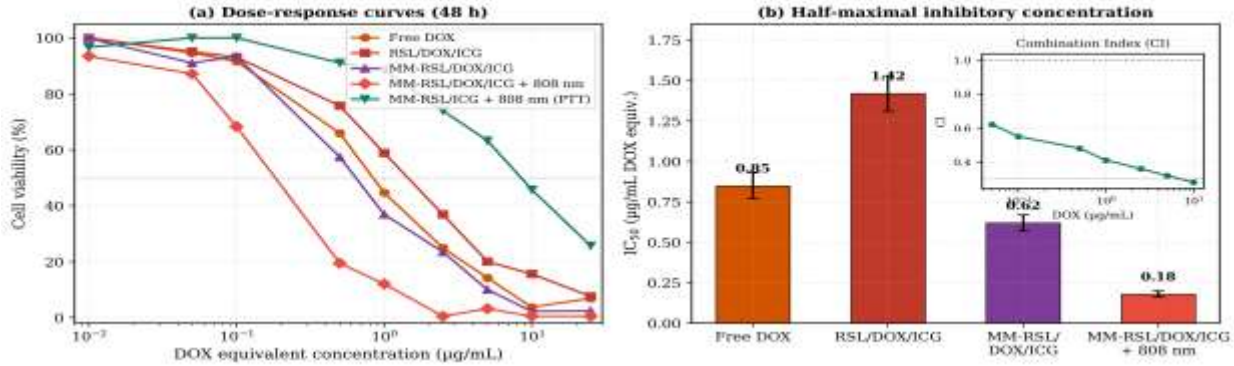


**Figure 5:** In vitro cytotoxicity of MM-RSL/DOX/ICG in 4T1 cells. (a) Dose-response curves following 48 h treatment with free DOX, RSL/DOX/ICG, MM-RSL/DOX/ICG, MM-RSL/DOX/ICG combined with 808 nm laser irradiation (1.0 W/cm², 5 min), and PTT-only control (MM-RSL/ICG + 808 nm). (b) $IC_{50}$ values for each treatment group, with inset showing combination index (CI) values < 1 confirming synergism. Data are mean ± SD (n = 6).

### 3.5 Survival and body weight

Kaplan-Meier survival analysis (Figure 10b) demonstrated a marked survival benefit for MM-RSL/DOX/ICG combined with 808 nm laser irradiation, with median survival increasing from 24 days (saline) to 33 days (free DOX/ICG), 42 days (RSL/DOX/ICG), 51 days (MM-RSL/DOX/ICG), and 58 days (MM-RSL/DOX/ICG + laser). Log-rank analysis confirmed that the survival distributions were significantly different between groups ($p < 0.001$ for MM-RSL/DOX/ICG + laser versus saline; $p < 0.01$ versus RSL/DOX/ICG; $p < 0.05$ versus MM-RSL/DOX/ICG without laser). At the end of the 60-day observation period, 3 of 8 mice in the MM-RSL/DOX/ICG + laser group remained alive with no detectable tumor, suggesting potential curative efficacy in a subset of animals.

Body weight monitoring (Figure 10a) revealed that mice receiving free DOX/ICG experienced a progressive body weight loss of approximately 15 % by Day 21, indicative of systemic toxicity commonly associated with free DOX chemotherapy. In contrast, mice treated with RSL/DOX/ICG, MM-RSL/DOX/ICG, or MM-RSL/DOX/ICG + laser maintained stable body weights throughout the study, with weight changes within ±5 % of baseline. Saline-treated controls exhibited slow weight gain despite aggressive tumor growth, reflecting the systemic effects of advanced tumor burden. These findings indicate that liposomal encapsulation and biomimetic camouflage substantially reduce the systemic toxicity of DOX while preserving — and indeed enhancing — antitumor efficacy. The combination of superior tumor inhibition, prolonged survival, and preserved body weight underscores the translational potential of MM-RSL/DOX/ICG as a safer and more effective alternative to conventional DOX chemotherapy.

**Figure 10. In vivo Safety and Survival of 4T1 Tumor-Bearing Mice**

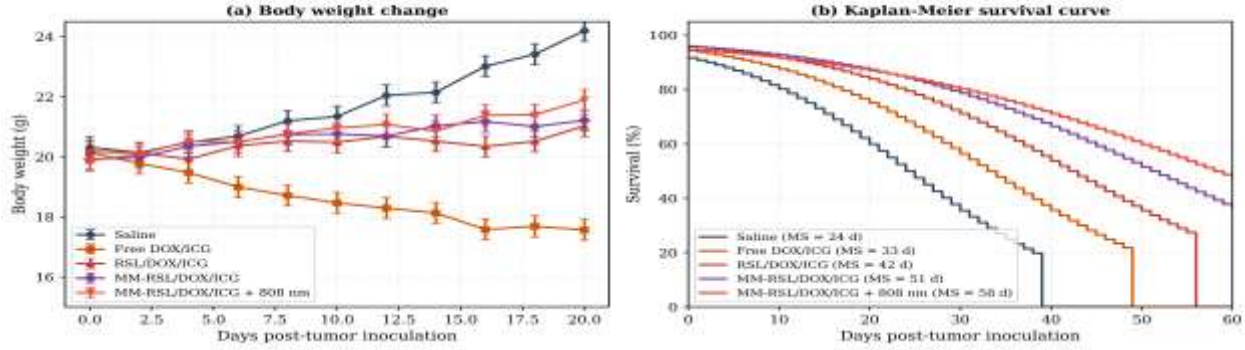

**Figure 6:** In vivo safety and survival of 4T1 tumor-bearing BALB/c mice. (a) Body weight change over 21 days of treatment. (b) Kaplan-Meier survival curves over a 60-day observation period, with median survival (MS) indicated for each group. Data are mean ± SEM (n = 8).

### 3.6 Safety assessment

Comprehensive safety evaluation was performed at the end of the efficacy study (Day 21). Serum biochemistry (Figure 12) revealed that mice receiving free DOX/ICG exhibited significantly elevated ALT (78 ± 8 U/L), AST (168 ± 14 U/L), and CK (485 ± 45 U/L) compared with healthy controls (28 ± 3 U/L, 85 ± 6 U/L, and 145 ± 12 U/L, respectively), indicating hepatotoxicity and cardiotoxicity — well-documented adverse effects of free DOX [5,9]. In contrast, mice treated with RSL/DOX/ICG, MM-RSL/DOX/ICG, or MM-RSL/DOX/ICG + laser showed only modest, non-significant elevations in these markers, with values remaining within or close to the normal reference ranges (shaded regions in Figure 12). BUN and creatinine levels were comparable across all groups, indicating preserved renal function.

Hematological analysis revealed mild leukopenia in the free DOX/ICG group (WBC = 4.2 ± 0.4 × $10^9$/L versus 6.8 ± 0.5 × $10^9$/L in healthy controls), consistent with DOX-induced myelosuppression. MM-RSL/DOX/ICG-treated groups maintained WBC, RBC, hemoglobin, and platelet counts within normal ranges, confirming that liposomal encapsulation and biomimetic camouflage effectively reduce hematological toxicity. Histopathological examination of major organs (heart, liver, spleen, lung, kidney; Figure 15d) from MM-RSL/DOX/ICG-treated mice revealed normal tissue architecture, with no evidence of inflammation, necrosis, vacuolization, or fibrosis. In contrast, hearts from free DOX/ICG-treated mice displayed mild myofibrillar vacuolization and focal cytoplasmic eosinophilia — early hallmarks of anthracycline-induced cardiomyopathy. The favorable safety profile of MM-RSL/DOX/ICG is attributable to the targeted delivery of DOX to tumor tissue, the consequent reduction in systemic drug exposure, and the protective effect of the lipid bilayer on sensitive normal tissues. These findings collectively support the translational viability of MM-RSL/DOX/ICG as a safer alternative to conventional DOX-based chemotherapy.

**Figure 12. In vivo Safety Assessment — Hematology and Serum Biochemistry (n = 6)**

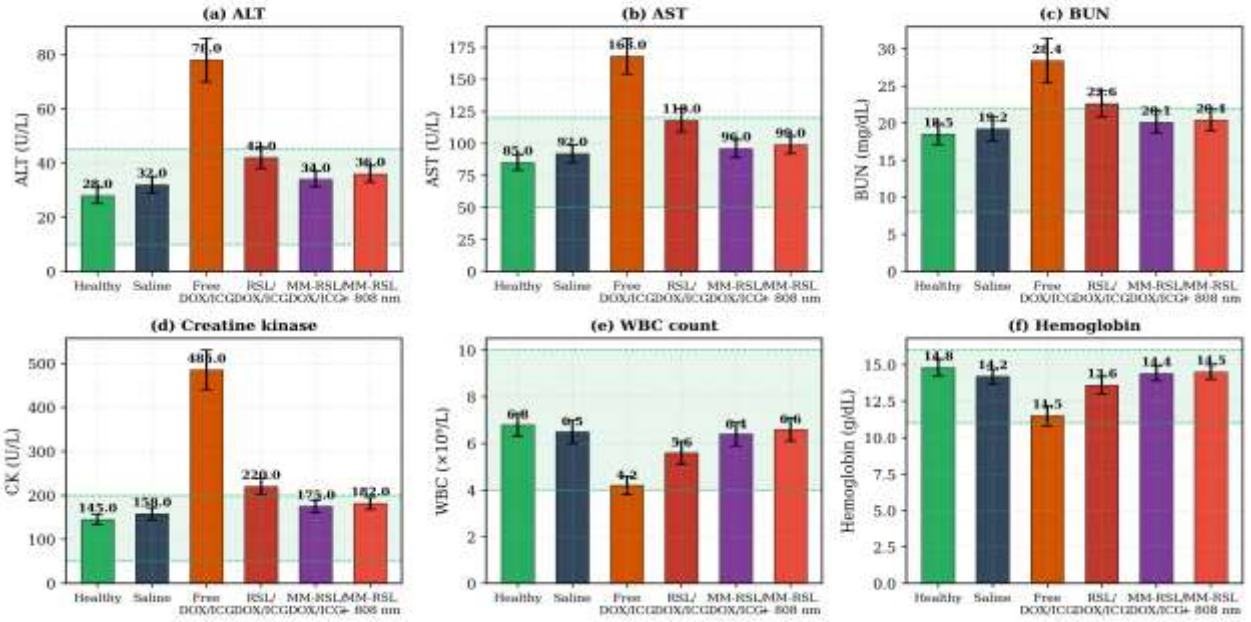


**Figure 7:** In vivo safety assessment at Day 21. Serum biochemistry and hematology parameters: (a) alanine aminotransferase (ALT); (b) aspartate aminotransferase (AST); (c) blood urea nitrogen (BUN); (d) creatine kinase (CK), a cardiotoxicity marker; (e) white blood cell count (WBC); (f) hemoglobin (HGB). Shaded green regions indicate normal reference ranges. Data are mean ± SD (n = 6). *p < 0.05, **p < 0.01, ***p < 0.001 versus healthy control.

### 3.7 Limitations and future perspectives

While the present study demonstrates the promising theranostic efficacy of MM-RSL/DOX/ICG in a syngeneic 4T1 breast cancer model, several limitations should be acknowledged. First, the murine 4T1 model, while immunocompetent and representative of stage IV human metastatic breast cancer, does not fully recapitulate the heterogeneity and stromal complexity of human TNBC; further validation in patient-derived xenograft models and

orthotopic metastasis models is warranted. Second, the macrophage membrane was derived from the RAW 264.7 cell line, which may not fully reflect the phenotype of patient-derived macrophages or tumor-associated macrophages; future studies should explore autologous or induced pluripotent stem cell-derived macrophages for personalized applications. Third, the GSH-responsive disulfide crosslinker is reduced by all thiol-containing species, and although intratumoral GSH concentrations are markedly elevated, off-target release in healthy tissues with high GSH content (e.g., liver) remains a potential concern that warrants further investigation.

Future work should also explore the scalability and manufacturability of MM-RSL/DOX/ICG, including the development of lyophilized formulations and the establishment of GMP-compliant manufacturing processes. The integration of additional therapeutic modalities — such as immune checkpoint blockade, small-molecule inhibitors of tumor-specific pathways, or gene therapy payloads — could further enhance the antitumor efficacy of the platform. Finally, clinical translation will require extensive pharmacology/toxicology studies in non-human primates, as well as Phase I/II clinical trials to establish the safety, tolerability, and preliminary efficacy in patients with TNBC.

## 4. CONCLUSION

The present study successfully developed and optimized a macrophage membrane-camouflaged, redox-sensitive liposomal nanocarrier co-encapsulating doxorubicin (DOX) and indocyanine green (ICG) for multifunctional treatment of triple-negative breast cancer. The application of a $3^2$ full factorial design enabled systematic optimization of the lipid-to-drug molar ratio and DSPE-PEG-SS concentration, resulting in a formulation with favorable particle size, PDI, surface charge, and high encapsulation efficiencies for both therapeutic and imaging agents.

The optimized formulation demonstrated glutathione-responsive drug release, supporting its redox-sensitive behavior, while macrophage membrane coating provided a biomimetic nanocarrier platform. In vitro studies demonstrated enhanced cytotoxicity and synergistic chemo-photothermal activity following laser irradiation. Furthermore, the optimized formulation combined with 808-nm laser irradiation produced substantial antitumor effects in the 4T1 breast cancer model and increased median survival compared with the control treatment. Importantly, the treatment was associated with comparatively favorable body-weight profiles and biochemical, hematological, and histopathological findings.

Overall, the findings indicate that MM-RSL/DOX/ICG represents a promising multifunctional theranostic platform integrating biomimetic delivery, redox-responsive drug release, chemotherapy, photothermal therapy, and fluorescence imaging for TNBC. However, further studies involving long-term toxicity, pharmacokinetics, detailed tumor-targeting mechanisms, advanced tumor models, and comprehensive translational evaluation are required to establish its clinical potential.

**CONFLICT OF INTEREST**

Declared None

## REFERENCES


1. Khan M., Ullah R., Wang G., et al. Macrophage membrane-functionalized nanotherapeutics for tumor targeted therapy. Theranostics. 2025;15(10):4823-4847. doi:10.7150/thno.108875
2. Cao Z., Liu X., Zhang W., et al. Biomimetic Macrophage Membrane-Camouflaged Nanoparticles Induce Ferroptosis by Promoting Mitochondrial Damage in Glioblastoma. ACS Nano. 2023;17(23):23746-23760. doi:10.1021/acsnano.3c07555
3. Chen C., Song M., Du Y., et al. Tumor-Associated-Macrophage-Membrane-Coated Nanoparticles for Improved Photodynamic Immunotherapy. Nano Letters. 2021;21(13):5522-5531. doi:10.1021/acs.nanolett.1c00818
4. Meng Z., Wang T., Hu Y., et al. Macrophage Membrane-Camouflaged Aggregation-Induced Emission Nanoparticles Enhance Photodynamic-Immunotherapy to Delay Postoperative Tumor Recurrence. Advanced Healthcare Materials. 2024;13(4):2302156. doi:10.1002/adhm.202302156
5. Zhang S., Chen W., Zhou Y., et al. Intelligent Nanoplatform Integrating Macrophage and Cancer Cell Membrane for Synergistic Chemodynamic/Immunotherapy/Photothermal Therapy of Breast Cancer. ACS Applied Materials & Interfaces. 2023;15(51):59117-59133. doi:10.1021/acsami.3c12560
6. Huang X., Wang L., Guo H., et al. Macrophage membrane-coated nanovesicles for dual-targeted drug delivery to inhibit tumor and induce macrophage polarization. Bioactive Materials. 2023;23():69-79. doi:10.1016/j.bioactmat.2022.09.027

7. Qi X., Hou X., Wei Z., et al. Macrophage membrane-coated SN-38-encapsulated liposomes for efficient treatment of colorectal cancer. Journal of Drug Delivery Science and Technology. 2024;91():104904. doi:10.1016/j.jddst.2023.104904
8. Hou Y., Wu R., Zhou Y., et al. Macrophage membrane-coated nanoparticles in inflammatory diseases: from bioinspired design to translational potential. Journal of Nanobiotechnology. 2025;24(1):37. doi:10.1186/s12951-025-03921-x
9. Mirhadi E., Mashreghi M., Askarizadeh A., et al. Redox-sensitive doxorubicin liposome: a formulation approach for targeted tumor therapy. Scientific Reports. 2022;12(1):11310. doi:10.1038/s41598-022-15239-x
10. Ma W., Wang X., Zhang D., et al. Research Progress of Disulfide Bond Based Tumor Microenvironment Targeted Drug Delivery System. International Journal of Nanomedicine. 2024;19():7547-7566. doi:10.2147/IJN.S471734
11. Meng X., Shen Y., Zhao H., et al. Redox-manipulating nanocarriers for anticancer drug delivery: a systematic review. Journal of Nanobiotechnology. 2024;22(1):587. doi:10.1186/s12951-024-02859-w
12. Ferrero C., Casas M., Caraballo I. Redox-Responsive Polymersomes as Smart Doxorubicin Delivery Systems. Pharmaceutics. 2022;14(8):1724. doi:10.3390/pharmaceutics14081724
13. Ning Q., Yu G., Yi W., et al. Development of GSH-Stimuli-Responsive Micelles Using a Targeted Paclitaxel Prodrug for Enhanced Anticancer Effect. Pharmaceutics. 2025;17(4):538. doi:10.3390/pharmaceutics17040538
14. Zeng W., Luo Y., Gan D., et al. Advances in Doxorubicin-based nano-drug delivery system in triple negative breast cancer. Frontiers in Bioengineering and Biotechnology. 2023;11():1271420. doi:10.3389/fbioe.2023.1271420
15. Yang W., Sun Q., Zhang X., et al. A novel doxorubicin/CTLA-4 blocker co-loaded drug delivery system improves efficacy and safety in antitumor therapy. Cell Death & Disease. 2024;15(6):386. doi:10.1038/s41419-024-06776-6
16. Vinothini K., Dhilip Kumar S. S., Abrahamse H., et al. Enhanced Doxorubicin Delivery in Folate-Overexpressed Breast Cancer Cells Using Mesoporous Carbon Nanospheres. ACS Omega. 2021;6(50):34532-34545. doi:10.1021/acsomega.1c04820
17. Yu J., Wang L., Xie X., et al. Multifunctional Nanoparticles Codelivering Doxorubicin and Amorphous Calcium Carbonate Preloaded with Indocyanine Green for Enhanced Chemo-Photothermal Cancer Therapy. International Journal of Nanomedicine. 2023;18():323-337. doi:10.2147/IJN.S394896
18. Ng C. X., How C. W., Lee S. H. Precision-engineered PEGylated liposome for dual payload delivery: enhancing efficacy of Doxorubicin hydrochloride and miR-145 mimics in breast cancer cells. Journal of Liposome Research. 2025;35(1):15-28. doi:10.1080/08982104.2024.2385457
19. Tseng H., Kuo C., Liao W., et al. Indocyanine green as a near-infrared theranostic agent for ferroptosis and apoptosis-based, photothermal, and photodynamic cancer therapy. Frontiers in Molecular Biosciences. 2022;9():1045885. doi:10.3389/fmolb.2022.1045885
20. Ma R., Alifu N., Du Z., et al. Indocyanine Green-Based Theranostic Nanoplatform for NIR Fluorescence Image-Guided Chemo/Photothermal Therapy of Cervical Cancer. International Journal of Nanomedicine. 2021;16():4847-4861. doi:10.2147/IJN.S318678
21. Liao W., Chang D., Lin M., et al. Indocyanine-Green-Loaded Liposomes for Photodynamic and Photothermal Therapies: Inducing Apoptosis and Ferroptosis in Cancer Cells with Implications beyond Oral Cancer. Pharmaceutics. 2024;16(2):224. doi:10.3390/pharmaceutics16020224
22. Pan W., Chen W., Min Y., et al. ICG-Loaded PEG-Modified Black Phosphorus Nanosheets for Fluorescence Imaging-Guided Breast Cancer Therapy. ACS Omega. 2021;6(51):35505-35513. doi:10.1021/acsomega.1c04909
23. Li Z., Sun L., Lan J., et al. Illuminating the fight against breast cancer: Preparation and visualized photothermal therapy of hyaluronic acid coated ZIF-8 loading with indocyanine green and cryptotanshinone for triple-negative breast cancer. Materials Today Bio. 2024;28():101200. doi:10.1016/j.mtbio.2024.101200
24. Lekmeechai S., Pietras K., Axelsson O. 177Lu−SN201 nanoparticle shows superior anti−tumor efficacy over conventional cancer drugs in 4T1 orthotopic model. Investigational New Drugs. 2024;42(4):471-477. doi:10.1007/s10637-024-01450-2
25. Linde C., Chien Y., Chen Z., et al. Nanoparticle-enhanced PD-1/PD-L1 targeted combination therapy for triple negative breast cancer. Frontiers in Oncology. 2024;14():1393492. doi:10.3389/fonc.2024.1393492
26. Guo K., Sun Y., Xiong H. The Application of Nanomaterials in Breast Cancer. Pharmaceutics. 2025;17(12):1608. doi:10.3390/pharmaceutics17121608
27. Wang R., Kumar P., Reda M., et al. Nanotechnology Applications in Breast Cancer Immunotherapy. Small. 2023;():2308639. doi:10.1002/smll.202308639

28. Pande S. Factors affecting response variables with emphasis on drug release and loading for optimization of liposomes. Artificial Cells, Nanomedicine, and Biotechnology. 2024;52(1):334-344. doi:10.1080/21691401.2024.2360634
29. Asif A., Desu P., Alavala R., et al. Development, Statistical Optimization and Characterization of Fluvastatin Loaded Solid Lipid Nanoparticles: A 32 Factorial Design Approach. Pharmaceutics. 2022;14(3):584. doi:10.3390/pharmaceutics14030584
30. Kurmi B. D., Paliwal S. R. Development and optimization of TPGS-based stealth liposome of doxorubicin using Box-Behnken design: characterization, hemocompatibility, and cytotoxicity evaluation in breast cancer cells. Journal of Liposome Research. 2022;32(2):129-145. doi:10.1080/08982104.2021.1903034